IEEE Photonics Journal
An IEEE Photonics Society Publication

Open Access

An Improved Subdomain Level Nonconformal Discontinuous Galerkin Time Domain (DGTD) Method for Materials With Full-Tensor Constitutive Parameters

Volume 9, Number 2, April 2017

Qiang Ren
Qiwei Zhan
Qing Huo Liu, *Fellow, IEEE*

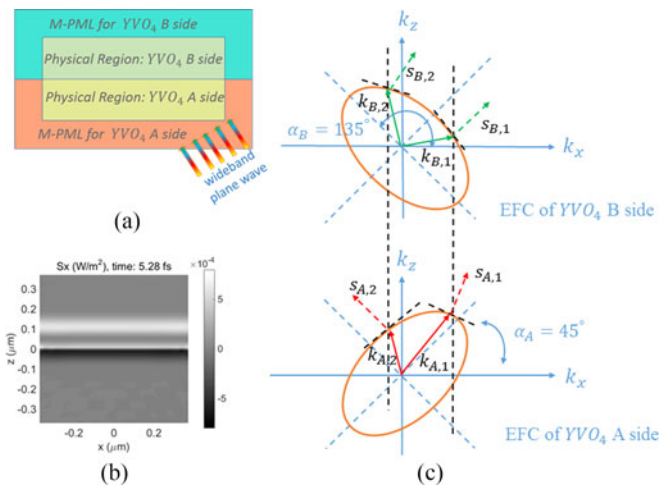

DOI: 10.1109/JPHOT.2017.2672644
1943-0655

An Improved Subdomain Level Nonconformal Discontinuous Galerkin Time Domain (DGTD) Method for Materials With Full-Tensor Constitutive Parameters

Qiang Ren,[1] **Qiwei Zhan,**[2] **and Qing Huo Liu,**[2] ***Fellow, IEEE***

[1]Department of Electrical Engineering, The Pennsylvania State University, University Park, PA 16802 USA
[2]Department of Electrical and Computer Engineering, Duke University, Durham, NC 27705 USA

DOI:10.1109/JPHOT.2017.2672644

Manuscript received June 22, 2016; revised February 14, 2017; accepted February 15, 2017. Date of publication February 22, 2017; date of current version March 21, 2017. Corresponding author: Q. H. Liu (e-mail: qhliu@duke.edu)

Abstract: Ultrawideband simulation of negative refraction in bicrystals is important for the design optimization of devices involving such anisotropic media, but it is a nontrivial task, especially when low-order methods are utilized. This work proposes an improved discontinuous Galerkin time domain (DGTD) method for simulating time-dependent electromagnetic fields for inhomogeneous media with full anisotropic constitutive parameters (full anisotropic media). It employs the electric field intensity **E** and magnetic flux density **B** to solve Maxwell's equations. The **EB**-scheme-based anisotropic Riemann solver and nonconformal mesh are employed for domain decomposition to allow efficient spatial discretization. An unsplit-field Maxwellian multiaxial perfectly matched layer for full anisotropic media is derived and shown to be effective to absorb outgoing waves and suppress the potential late-time instability found in classical PML. In addition, the total-field/scattered-field technique is further studied to allow a nonconformal mesh, vector basis functions, and half-space situation. This newly improved DGTD method is validated with test cases and applied to the negative reflection in YVO_4 bicrystal.

Index Terms: Discontinuous Galerkin time domain (DGTD) method, multiaxial PML (M-PML), non-conformal mesh, negative refraction, YVO_4 bicrystal

1. Introduction

A bicrystal is formed by two adjacent crystals of different orientations separated by a grain boundary. It is widely used in optical devices as refraction and reflection can be steered at the interface. Recently, more research of the amphoteric-refracting medium consisting of bicrystals has been conducted as it can realize the negative refraction in conventional crystals other than metamaterials [1], [2].

Ultra wideband time domain simulation of bicrystals is a challenging problem, especially when its background is also a half space anisotropic medium. To the best knowledge of the authors, no 3-D time domain solvers have been reported for the simulation of the negative refraction in bicrystals. The difficulties lie in the following aspects: a much larger stencil in the finite-difference time domain (FDTD) method for full anisotropy than for isotropic media; a large mass matrix for an anisotropic

medium, absorbing boundary condition, and plane-wave source implementation. To address these difficulties, we propose the anisotropic discontinuous Galerkin time domain (DGTD) method in this paper. As an extension of the isotropic subdomain level DGTD method in [3]–[6], it inherits many advantages, including the non-conformal mesh that can alleviate meshing difficulties for large scale problems, the **EB** scheme that is more efficient than the **EH** scheme, multiple kinds of elements.

To handle the anisotropy (especially the full anisotropy) in bicrystals, this proposed method casts the anisotropic Riemann solver (upwind flux) in [7] to the **EB** form to fulfill the domain decomposition. The open boundary condition in this anisotropic DGTD method is based on the perfectly matched layer (PML) technique. PML is the most popular frequency-independent absorbing boundary condition to attenuate out-going waves at all incidence angles. However, most of the PMLs aim at matching isotropic media, even though the media in the PML region can be anisotropic [8], [9]. To match full anisotropic media, the rare time domain PML includes the work in [10]–[12], all of which use split-field formulations, thus they are not suitable for the finite element method (FEM). In this paper, we propose an unsplit-field time domain PML to match full anisotropic media. As a follow-up work of [13], this anisotropic PML also has a Maxwellian form. To suppress the late time instability associated with the anisotropy, it is further modified to multiaxial PML (M-PML) at the cost of simply adding additional damping profiles.

In addition, for the source implementation, the conventional total-field/scatter-field (TF/SF) technique for a homogeneous isotropic background medium is extended to a full anisotropic half space; it allows the vector basis functions and non-conformal mesh, thus the plane wave excitation can be incorporated in this DGTD method for bicrystals.

The new contributions of this paper are as follows: first, it proposes a non-convolutional, unsplit-field, stable multiaxial PML in the time domain for full anisotropic media for the first time; second, it carries out the TF/SF technique for vector basis functions in non-conformal mesh for wideband incident plane waves; last, after the above non-conformal TF/SF technique is extended to a half-space configuration, the negative refraction phenomenon in YVO_4 bicrystal is simulated successfully in the time domain for the first time with the anisotropic DGTD method.

2. Methods and Formulations

2.1 EB Scheme Anisotropic Riemann Solver

The weak form of the **EB** scheme Maxwell's equations after testing are [14]

$$\int_V \mathbf{\Phi}^i \cdot \left(\frac{\partial \bar{\bar{\epsilon}} \mathbf{E}^i}{\partial t} + \bar{\bar{\sigma}}_e \mathbf{E}^i + \mathbf{J}^i \right) dV = \int_V \nabla \times \mathbf{\Phi}^i \cdot \bar{\bar{\mu}}^{-1} \mathbf{B}^i dV + \int_S \mathbf{\Phi}_p^i \cdot (\hat{\mathbf{n}}^i \times \bar{\bar{\mu}}^{-1} \mathbf{B}^t) dS \tag{1}$$

$$\int_V \mathbf{\Psi}^i \cdot \left(\frac{\partial \mathbf{B}^i}{\partial t} + \bar{\bar{\sigma}}_m \bar{\bar{\mu}}^{-1} \mathbf{B}^i + \mathbf{M}^i \right) dV = -\int_V \mathbf{\Psi}^i \cdot \nabla \times \mathbf{E}^i dV + \int_S \mathbf{\Psi}^i \cdot (\hat{\mathbf{n}}^i \times \mathbf{E}^i) dS - \int_S \mathbf{\Psi}^i \cdot (\hat{\mathbf{n}}^i \times \mathbf{E}^t) dS \tag{2}$$

where $\bar{\bar{\epsilon}}$, $\bar{\bar{\mu}}$, $\bar{\bar{\sigma}}_e$, and $\bar{\bar{\sigma}}_m$ are all 3×3 tensors denoting the material's permittivity, permeability, electric and magnetic conductivities, respectively; **J** and **M** are the imposed electric and magnetic current density sources. The testing curl-conforming and divergence-conforming basis functions $\mathbf{\Phi}$ and $\mathbf{\Psi}$ can be found in [3], [4], and [15]. Superscripts i, j and t denote local, adjacent, and total field quantities, respectively, and $\hat{\mathbf{n}}$ is the outward normal vector. Note that integration by parts is applied once in (1), but twice in (2), because we prefer the curl operator functioning on the curl-conforming basis functions. Similar techniques are also used for nodal DG finite element and spectral element methods for hyperbolic systems [16]–[18].

The terms $\hat{\mathbf{n}}^i \times \bar{\bar{\mu}}^{-1} \mathbf{B}^t$ and $\hat{\mathbf{n}}^i \times \mathbf{E}^t$ in the surface integrations in (1) and (2) are the numerical fluxes which are introduced to relax the continuity condition of tangential intensity fields. Because the continuity condition is strict which requires solving the whole linear system together [19], it hinders domain decomposition. The key point of the DG method is how to calculate this flux. Here we adopt the anisotropic Riemann solver from [7] while replacing field variable **H** with **B**:

$$(\hat{\mathbf{n}}^i \times \bar{\bar{\mu}}^{-1} \mathbf{B}^t) = \mathbf{T}^{-1} (\mathbf{Z}^i + \mathbf{Z}^j)^{-1} [\mathbf{Z}^j \mathbf{T} (\hat{\mathbf{n}}^i \times (\bar{\bar{\mu}}^i)^{-1} \mathbf{B}^i) + \mathbf{Z}^j \mathbf{T} (\hat{\mathbf{n}}^i \times (\bar{\bar{\mu}}^j)^{-1} \mathbf{B}^j) - \mathbf{T} (\hat{\mathbf{n}}^i \times \hat{\mathbf{n}}^i \times (\mathbf{E}^j - \mathbf{E}^i))] \tag{3}$$

$$(\hat{\mathbf{n}}^i \times \mathbf{E}^t) = \mathbf{T}^{-1}(\mathbf{Y}^i + \mathbf{Y}^j)^{-1}[\mathbf{Y}^i\mathbf{T}(\hat{\mathbf{n}}^i \times \mathbf{E}^i) + \mathbf{Y}^j\mathbf{T}(\hat{\mathbf{n}}^i \times \mathbf{E}^j) + \mathbf{T}(\hat{\mathbf{n}}^i \times \hat{\mathbf{n}}^i \times ((\bar{\bar{\mu}}^j)^{-1}\mathbf{B}^j - (\bar{\bar{\mu}}^i)^{-1}\mathbf{B}^i))] \quad (4)$$

where $\bar{\bar{\mu}}^i$ and $\bar{\bar{\epsilon}}^i$ are the relative permeability and permittivity of the ith subdomain, respectively. **Y** and **Z** follow the definitions in [7], and **T** is the transformation matrix between local and global coordinates. In isotropic media, we do not need to use **T** because the admittance and impedance are scalars instead of tensors, thus **T** and $\mathbf{T}^{-1}$ cancel each other in (3) and (4).

The system matrices in (1) and (2) from the volume integrations have the same expressions as those for isotropic media [3], [4], except that the constitutive parameters are tensors. However, the matrices from surface integration, which are related with the Riemann solver, are different:

$$(\mathbf{L}_{eb}^{ij})_{pq} = \langle \mathbf{\Phi}_p^i \ , \ \mathbf{T}^{-1}(\mathbf{Z}_i + \mathbf{Z}_j)^{-1}(\mathbf{Z}_j\mathbf{T}(\hat{\mathbf{n}}^i \times \hat{\mathbf{n}}^i \times (\bar{\bar{\mu}}^j)^{-1}\mathbf{\Psi}_q^j))\rangle_{S_{ij}} \quad (i \neq j) \quad (5)$$

$$(\mathbf{L}_{be}^{ij})_{pq} = -\langle \mathbf{\Psi}_p^i \ , \ \mathbf{T}^{-1}(\mathbf{Y}_i + \mathbf{Y}_j)^{-1}(\mathbf{Y}_j\mathbf{T}(\hat{\mathbf{n}}^i \times \hat{\mathbf{n}}^i \times \mathbf{\Phi}_q^j))\rangle_{S_{ij}} \quad (i \neq j) \quad (6)$$

$$(\mathbf{L}_{eb}^{ii})_{pq} = \sum_{j=1}^{N} \langle \mathbf{\Phi}_p^i \ , \ \mathbf{T}^{-1}(\mathbf{Z}_i + \mathbf{Z}_j)^{-1}(\mathbf{Z}_j\mathbf{T}(\hat{\mathbf{n}}^i \times \hat{\mathbf{n}}^i \times (\bar{\bar{\mu}}^i)^{-1}\mathbf{\Psi}_q^i))\rangle_{S_{ij}} \quad (7)$$

$$(\mathbf{L}_{be}^{ii})_{pq} = \sum_{j=1}^{N} \langle \mathbf{\Psi}_p^i \ , \ \mathbf{T}^{-1}(\mathbf{Y}_i + \mathbf{Y}_i)^{-1}(\mathbf{Y}_j\mathbf{T}(\hat{\mathbf{n}}^i \times \hat{\mathbf{n}}^i \times \mathbf{\Phi}_q^i))\rangle_{S_{ij}} \quad (8)$$

$$(\mathbf{L}_{ee}^{ij})_{pq} = \langle \mathbf{\Phi}_p^i \ , \ \mathbf{T}^{-1}(\mathbf{Z}_i + \mathbf{Z}_j)^{-1}\mathbf{T}(\hat{\mathbf{n}}^i \times \hat{\mathbf{n}}^i \times \mathbf{\Phi}_q^j)\rangle_{S_{ij}} \quad (i \neq j) \quad (9)$$

$$(\mathbf{L}_{bb}^{ij})_{pq} = -\langle \mathbf{\Psi}_p^i \ , \ \mathbf{T}^{-1}(\mathbf{Y}_i + \mathbf{Y}_j)^{-1}\mathbf{T}(\hat{\mathbf{n}}^i \times \hat{\mathbf{n}}^i \times (\bar{\bar{\mu}}^j)^{-1}\mathbf{\Psi}_q^j)\rangle_{S_{ij}} \quad (i \neq j) \quad (10)$$

$$(\mathbf{L}_{ee}^{ii})_{pq} = \sum_{j=1}^{N} \langle \mathbf{\Phi}_p^i \ , \ \mathbf{T}^{-1}(\mathbf{Z}_i + \mathbf{Z}_j)^{-1}\mathbf{T}(\hat{\mathbf{n}}^i \times \hat{\mathbf{n}}^i \times \mathbf{\Phi}_q^i)\rangle_{S_{ij}} \quad (11)$$

$$(\mathbf{L}_{bb}^{ii})_{pq} = \sum_{j=1}^{N} \langle \mathbf{\Psi}_p^i, \mathbf{T}^{-1}(\mathbf{Y}_i + \mathbf{Y}_j)^{-1}\mathbf{T}(\hat{\mathbf{n}}^i \times \hat{\mathbf{n}}^i \times (\bar{\bar{\mu}}^i)^{-1}\mathbf{\Psi}_q^i)\rangle_{S_{ij}} \quad (12)$$

where S_{ij} is the interface between the ith and jth subdomains, and $\langle \mathbf{f}, \mathbf{g}\rangle_{S_{ij}} = \int_{S_{ij}} \mathbf{f}^T \cdot \mathbf{g} dS$. Subscripts p and q are the local indexes of basis functions.

2.2 The EB Scheme PML and M-PML for Anisotropic Media

A non-convolutional, unsplit-field Maxwellian PML is proposed here to match full anisotropic media. This PML can be viewed as an extension of the work in [13]. First, we apply the complex coordinate-stretching variables to Maxwell's equations while assuming the permeability, permittivity, electric and magnetic conductivities are tensors

$$\partial\eta \rightarrow \left[1 + \frac{\omega_\eta(\eta)}{j\omega}\right]\partial\eta \quad (\eta = x, y, z) \quad (13)$$

where ω_η is the attenuation coefficient in the direction η ($\eta = x, y, z$). For simplicity but without loss generality, we just consider the z component of Faraday's and Ampere's laws as follows:

$$\frac{\partial(\bar{\bar{\epsilon}}\mathbf{E})_z}{\partial t} = \frac{\partial(\bar{\bar{\mu}}^{-1}\mathbf{B})_y}{\partial x} - \frac{\partial(\bar{\bar{\mu}}^{-1}\mathbf{B})_x}{\partial y} - (\bar{\bar{\sigma}}_e\mathbf{E})_z, \quad \frac{\partial\mathbf{B}_z}{\partial t} = \frac{\partial\mathbf{E}_x}{\partial y} - \frac{\partial\mathbf{E}_y}{\partial x} - (\bar{\bar{\sigma}}_m\bar{\bar{\mu}}^{-1}\mathbf{B})_z. \quad (14)$$

With (13) and the transformation $\frac{\partial}{\partial t} \to j\omega$, (14) can be expanded in the frequency domain as

$$j\omega(\bar{\bar{\epsilon}}\mathbf{E})_z + (\omega_x+\omega_y)(\bar{\bar{\epsilon}}\mathbf{E})_z + (\bar{\bar{\sigma}}_e\mathbf{E})_z + \frac{\omega_x\omega_y(\bar{\bar{\epsilon}}\mathbf{E})_z + (\omega_x+\omega_y)(\bar{\bar{\sigma}}_e\mathbf{E})_z}{j\omega} + \frac{\omega_x\omega_y(\bar{\bar{\sigma}}_e\mathbf{E})_z}{(j\omega)^2}$$
$$= \frac{\partial}{\partial x}\left(1+\frac{\omega_y}{j\omega}\right)(\bar{\bar{\mu}}^{-1}\mathbf{B})_y - \frac{\partial}{\partial y}\left(1+\frac{\omega_x}{j\omega}\right)(\bar{\bar{\mu}}^{-1}\mathbf{B})_x \tag{15}$$

$$j\omega\mathbf{B}_z + (\omega_x+\omega_y)\mathbf{B}_z + (\bar{\bar{\sigma}}_m\bar{\bar{\mu}}^{-1}\mathbf{B})_z + \frac{\omega_x\omega_y\mathbf{B}_z + (\omega_x+\omega_y)(\bar{\bar{\sigma}}_m\bar{\bar{\mu}}^{-1}\mathbf{B})_z}{j\omega} + \frac{\omega_x\omega_y(\bar{\bar{\sigma}}_e\bar{\bar{\mu}}^{-1}\mathbf{B})_z}{(j\omega)^2}$$
$$= \frac{\partial}{\partial x}\left(1+\frac{\omega_y}{j\omega}\right)\mathbf{E}_y - \frac{\partial}{\partial y}\left(1+\frac{\omega_x}{j\omega}\right)\mathbf{E}_x. \tag{16}$$

Similarly to (14), we can obtain the equations for the x and y components.

Denote $\frac{\partial\mathbf{E}^{(1)}}{\partial t} = \tilde{\mathbf{E}}$, $\frac{\partial\mathbf{E}^{(2)}}{\partial t} = \mathbf{E}^{(1)}$, $\frac{\partial\mathbf{B}^{(1)}}{\partial t} = \tilde{\mathbf{B}}$, $\frac{\partial\mathbf{B}^{(2)}}{\partial t} = \mathbf{B}^{(1)}$ and define the auxiliary variables as

$$\tilde{\mathbf{E}}_\eta = \mathbf{E}_\eta + \omega_\eta\mathbf{E}^{(1)}_\eta, \quad (\bar{\bar{\mu}}^{-1}\tilde{\mathbf{B}})_\eta = (\bar{\bar{\mu}}^{-1}\mathbf{B})_\eta + \omega_\eta(\bar{\bar{\mu}}^{-1}\mathbf{B}^{(1)})_\eta \quad (\eta = x, y, z) \tag{17}$$

$$\mathbf{\Lambda}_0 = \mathrm{diag}\{\omega_x, \omega_y, \omega_z\}, \quad \mathbf{\Lambda}_1 = \mathrm{diag}\{\omega_y+\omega_z, \omega_z+\omega_x, \omega_x+\omega_y\}, \quad \mathbf{\Lambda}_2 = \mathrm{diag}\{\omega_y\omega_z, \omega_z\omega_x, \omega_x\omega_y\} \tag{18}$$

then the **EB** scheme compact form of Maxwell's equations in the PML region can be obtained by transforming back from frequency domain to time domain, which are shown as follows:

$$\nabla\times\tilde{\mathbf{E}} = -\frac{\partial\tilde{\mathbf{B}}}{\partial t} - (\bar{\bar{\sigma}}_m\bar{\bar{\mu}}^{-1} + \mathbf{\Lambda}_1 + \bar{\bar{\mu}}\mathbf{\Lambda}_0\bar{\bar{\mu}}^{-1})\tilde{\mathbf{B}} - \mathbf{\Lambda}_2\bar{\bar{\sigma}}_m\bar{\bar{\mu}}^{-1}\mathbf{B}^{(2)} - (\mathbf{\Lambda}_1\bar{\bar{\sigma}}_m\bar{\bar{\mu}}^{-1} - \bar{\bar{\sigma}}_m\mathbf{\Lambda}_0\bar{\bar{\mu}}^{-1}$$
$$+ \bar{\bar{\mu}}\mathbf{\Lambda}_0^2\bar{\bar{\mu}}^{-1} - \mathbf{\Lambda}_1\bar{\bar{\mu}}\mathbf{\Lambda}_0\bar{\bar{\mu}}^{-1} + \mathbf{\Lambda}_2)\mathbf{B}^{(1)} \tag{19}$$

$$\nabla\times\bar{\bar{\mu}}^{-1}\tilde{\mathbf{B}} = \frac{\partial\bar{\bar{\epsilon}}\tilde{\mathbf{E}}}{\partial t} + (\bar{\bar{\sigma}}_e + \mathbf{\Lambda}_1\bar{\bar{\epsilon}} + \bar{\bar{\epsilon}}\mathbf{\Lambda}_0)\tilde{\mathbf{E}} + \mathbf{\Lambda}_2\bar{\bar{\sigma}}_e\mathbf{E}^{(2)} + (\mathbf{\Lambda}_1\bar{\bar{\sigma}}_e - \bar{\bar{\sigma}}_e\mathbf{\Lambda}_0 + \bar{\bar{\epsilon}}\mathbf{\Lambda}_0^2 - \mathbf{\Lambda}_1\bar{\bar{\epsilon}}\mathbf{\Lambda}_0 + \mathbf{\Lambda}_2\bar{\bar{\epsilon}})\mathbf{E}^{(1)}. \tag{20}$$

and the auxiliary ordinary differential equations are

$$\frac{\partial\mathbf{E}^{(1)}}{\partial t} = \tilde{\mathbf{E}} - \mathbf{\Lambda}_0\mathbf{E}^{(1)}, \quad \frac{\partial\mathbf{E}^{(2)}}{\partial t} = \mathbf{E}^{(1)}, \quad \frac{\partial\mathbf{B}^{(1)}}{\partial t} = \tilde{\mathbf{B}} - \bar{\bar{\mu}}\mathbf{\Lambda}_0\bar{\bar{\mu}}^{-1}\mathbf{B}^{(1)}, \quad \frac{\partial\mathbf{B}^{(2)}}{\partial t} = \mathbf{B}^{(1)} \tag{21}$$

The auxiliary equations in (21) for the PML region are totally local and the profile parameters are only related with the volume integration, not with the Riemann solver. Therefore, the upwind flux aforementioned applies to not only the physical regions but also the PML regions. The extra work in the PML regions, which includes calculating the additional damping terms and updating the auxiliary ordinary differential equations, is not cumbersome. The system equations are

$$\mathbf{M}^i_{ee}\frac{d\tilde{\mathbf{e}}^i}{dt} = \mathbf{K}^i_{eb}\tilde{\mathbf{b}}^i + \mathbf{R}^i_{ee}\tilde{\mathbf{e}}^i + \mathbf{S}^i_{ee}(\mathbf{e}^{(1)})^i + \mathbf{W}^i_{ee}(\mathbf{e}^{(2)})^i + \mathbf{j}^i + \sum_{j=1}^{N}\mathbf{L}^{ij}_{eb}\tilde{\mathbf{b}}^j + \sum_{j=1}^{N}\mathbf{L}^{ij}_{ee}\tilde{\mathbf{e}}^j \tag{22}$$

$$\mathbf{M}^i_{bb}\frac{d\tilde{\mathbf{b}}^i}{dt} = \mathbf{K}^i_{be}\tilde{\mathbf{e}}^i + \mathbf{R}^i_{bb}\tilde{\mathbf{b}}^i + \mathbf{S}^i_{bb}(\mathbf{b}^{(1)})^i + \mathbf{W}^i_{bb}(\mathbf{b}^{(2)})^i + \mathbf{m}^i + \sum_{j=1}^{N}\mathbf{L}^{ij}_{be}\tilde{\mathbf{e}}^j + \sum_{j=1}^{N}\mathbf{L}^{ij}_{bb}\tilde{\mathbf{b}}^j \tag{23}$$

$$\mathbf{M}^i_{ee}\frac{d(\mathbf{e}^{(1)})^i}{dt} = \mathbf{M}^i_{ee}\tilde{\mathbf{e}}^i + \mathbf{T}^i_{ee}(\mathbf{e}^{(1)})^i, \quad \mathbf{M}^i_{bb}\frac{d((\mathbf{b}^{(1)})^i}{dt} = \mathbf{M}^i_{bb}\tilde{\mathbf{b}}^i + \mathbf{T}^i_{bb}(\mathbf{b}^{(1)})^i \tag{24}$$

where $\tilde{\mathbf{e}}$, $\mathbf{e}^1$, $\mathbf{e}^{(2)}$, $\tilde{\mathbf{b}}$, $\mathbf{b}^{(1)}$, and $\mathbf{b}^{(2)}$ are the unknown vectors. The mass and stiffness matrices ($\mathbf{M}_{ee}$, $\mathbf{M}_{bb}$, $\mathbf{K}_{be}$, and $\mathbf{K}_{eb}$) can be found in [4], except the difference that the constitutive parameters are

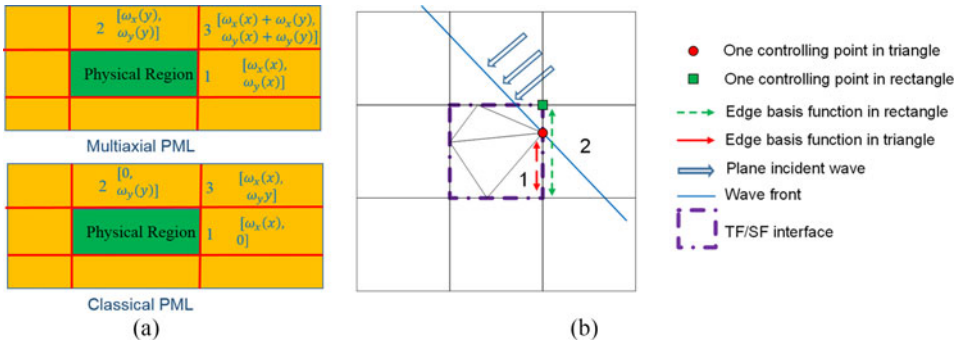

Fig. 1. (a) Attenuation parameters in classic PML and multiaxial PML. (b) Total-field/scattered-field (TF/SF) technique for a non-conformal mesh.

tensors. **L** matrices are defined in (5)–(12). The damping matrices are listed as follows:

$$(\mathbf{R}_{ee})_{pq} = -\langle \mathbf{\Phi}_p, (\bar{\bar{\sigma}}_e + \mathbf{\Lambda}_1\bar{\bar{\epsilon}} + \bar{\bar{\epsilon}}\mathbf{\Lambda}_0)\mathbf{\Phi}_q\rangle_{V_e}, \quad (\mathbf{W}_{ee})_{pq} = -\langle \mathbf{\Phi}_p, \mathbf{\Lambda}_2\bar{\bar{\sigma}}_e\mathbf{\Phi}_q\rangle_{V_e} \tag{25}$$

$$(\mathbf{S}_{ee})_{pq} = -\langle \mathbf{\Phi}_p, (\mathbf{\Lambda}_1\bar{\bar{\sigma}}_e - \bar{\bar{\sigma}}_e\mathbf{\Lambda}_0 + \bar{\bar{\epsilon}}\mathbf{\Lambda}_0^2 - \mathbf{\Lambda}_1\bar{\bar{\epsilon}}\mathbf{\Lambda}_0 + \mathbf{\Lambda}_2\bar{\bar{\epsilon}})\mathbf{\Phi}_q\rangle_{V_e}, \quad (\mathbf{T}_{ee})_{pq} = -\langle \mathbf{\Phi}_p, \mathbf{\Lambda}_0\mathbf{\Phi}_q\rangle_{V_e} \tag{26}$$

$$(\mathbf{R}_{bb})_{pq} = -\langle \mathbf{\Psi}_p, (\bar{\bar{\sigma}}_m\bar{\bar{\mu}}^{-1} + \mathbf{\Lambda}_1 + \bar{\bar{\mu}}\mathbf{\Lambda}_0\mu^{-1})\mathbf{\Psi}_q\rangle_{V_e}, \quad (\mathbf{W}_{bb})_{pq} = -\langle \mathbf{\Psi}_p, \mathbf{\Lambda}_2\bar{\bar{\sigma}}_m\bar{\bar{\mu}}^{-1}\mathbf{\Psi}_q\rangle_{V_e} \tag{27}$$

$$(\mathbf{S}_{bb})_{pq} = -\langle \mathbf{\Psi}_p, (\mathbf{\Lambda}_1\bar{\bar{\sigma}}_m\bar{\bar{\mu}}^{-1} - \bar{\bar{\sigma}}_m\mathbf{\Lambda}_0\bar{\bar{\mu}}^{-1} + \bar{\bar{\mu}}\mathbf{\Lambda}_0^2\bar{\bar{\mu}}^{-1} - \mathbf{\Lambda}_1\bar{\bar{\mu}}\mathbf{\Lambda}_0\bar{\bar{\mu}}^{-1} + \mathbf{\Lambda}_2)\mathbf{\Psi}_q\rangle_{V_e}$$

$$(\mathbf{T}_{bb})_{pq} = -\langle \mathbf{\Psi}_p, \bar{\bar{\mu}}\mathbf{\Lambda}_0\bar{\bar{\mu}}^{-1}\mathbf{\Psi}_q\rangle_{V_e}. \tag{28}$$

The time stepping scheme employed throughout this paper is the explicit fourth order Runge-Kutta (RK4) [4], [6], [14]. To remove of the potential late-time instability in classical anisotropic PML, Meza-Fajardo and Papageorgiou introduced the multiaxial PML (M-PML) in a split form for FDTD in elastic wave propagation [20]. M-PML is further discussed and developed in [21], [22]. The idea of M-PML is to add small damping profiles in all directions. Only slight modification is needed to obtain M-PML from classical PML as shown in Fig. 1(a) for the 2-D version.

The attenuation in the direction η ($\eta = x, y$) is described by ω_η. In the classical PML, damping only exists in the direction perpendicular to the interface between the physical region and PML. For example, area 1 has damping in the x direction, but not in the y direction. However, in M-PML, the damping profiles in area 1 include both x and y directions as functions of x, which are denoted as $\omega_x(x)$ and $\omega_y(x)$, respectively. The additional term $\omega_y(x)$ can be proportional to $\omega_x(x)$ and the ratio is defined as $r(y, x)$. For area 2, the damping profiles are $\omega_x(y)$ and $\omega_y(y)$. The damping profiles in the corner area 3 are added from adjacent areas 1 and 2.

Similar to the 2-D case, a ratio matrix **R** can be defined to obtain the damping profiles in the 3-D M-PML region from the classical PML:

$$\begin{bmatrix} \omega'_x \\ \omega'_y \\ \omega'_z \end{bmatrix} = \mathbf{R}\begin{bmatrix} \omega_x \\ \omega_y \\ \omega_z \end{bmatrix} = \begin{bmatrix} 1 & r(x,y) & r(x,z) \\ r(y,x) & 1 & r(y,z) \\ r(z,x) & r(z,y) & 1 \end{bmatrix}\begin{bmatrix} \omega_x \\ \omega_y \\ \omega_z \end{bmatrix}. \tag{29}$$

The M-PML requires simply replacing ω_η in (17) with ω'_η based on the classical PML. Note that the M-PML is not a strictly perfectly matching condition [23], and a small spurious numerical reflection exists between the physical region and M-PML. However, we can set the off-diagonal elements in **R** small to minimize the reflection. Usually, $r(\xi, \zeta) = 0.05 \quad (\xi, \zeta = x, y, z, \quad \xi \neq \zeta)$ is enough to suppress the instability, which is employed in the following simulations.

2.3 TF/SF Technique for Vector Basis Functions With Non-Conformal Mesh

Before showing the numerical results for an actual application, a TF/SF technique is presented for the plane wave incidence at the physical region adjacent to the M-PML truncation. (Note that all the following procedures for the TF/SF technique also apply to classical PML.) We use the scattered and total fields as the unknowns for the M-PML and the physical regions, respectively. The TF/SF interface is just the same as the shared face between the M-PML and physical region with non-conformal mesh.

A 2-D sketch of this technique is illustrated in Fig. 1(b). Every basis function has a control point, where its value is maximal. Assume $\mathbf{v}_i = [e_{i,1}, \cdots, e_{i,m}, b_{i,1}, \cdots, b_{i,n}]^T$ and $\mathbf{v}_j = [e_{j,1}, \cdots, e_{j,k}, b_{j,1}, \cdots, b_{j,l}]^T$ are the unknown vectors for a physical subdomain and its adjacent M-PML subdomain, respectively. T denotes the transpose of a vector, e and b are the unknowns, and the DoFs for the ith and jth subdomains are $(m+n)$ and $(k+l)$, respectively.

As the M-PML region including its interface uses the scattered field, the incident plane wave needs to be added here to obtain the total field (then coupled with the total field in the physical subdomain via Riemann solver). The incident wave is projected to the basis functions in the jth subdomain, and forms an "incident vector" $\mathbf{v}_{j,inc} = [e_{inc,1}, \cdots, e_{inc,k}, b_{inc,1}, \cdots, b_{inc,l}]^T$, where $e_{inc,p} = \langle \mathbf{E}_{inc}, \mathbf{\Phi}_{j,p} \rangle$ and $b_{inc,p} = \langle \mathbf{B}_{inc}, \mathbf{\Psi}_{j,p} \rangle$. $\mathbf{E}_{inc}$ and $\mathbf{B}_{inc}$ are the incident electric field intensity and magnetic flux density, while $\mathbf{\Phi}$ and $\mathbf{\Psi}$ are the basis functions for $\mathbf{E}$ and $\mathbf{B}$.

Assume the wave speed in this anisotropic medium is c (either ordinary wave speed or extraordinary wave speed), $f(t)$ is the time function of the plane wave, and $r_{i,p}$ is the distance from the pth control point in the ith subdomain to the plane wave front at the time $t = 0$. Then the time-varying illumination matrix is defined as

$$\mathbf{F}_i = \text{diag}\left\{ f\left(t - \frac{r_{i,1}}{c}\right), \cdots, f\left(t - \frac{r_{i,m+n}}{c}\right) \right\} \tag{30}$$

and the system equation for the local subdomain with the TF/SF technique is

$$\mathbf{M}_i \frac{d\mathbf{v}_i}{dt} = \mathbf{L}_{ii}\mathbf{v}_i + \sum_j \mathbf{L}_{ij}\mathbf{v}_j + \mathbf{F}_i \sum_j \mathbf{L}_{ij}\mathbf{v}_{j,inc}. \tag{31}$$

That means the time at which to add the incident wave is controlled by the locations of the control points in the local subdomain, and it has no relation with any information from its adjacent subdomains. However, the quantity of flux added to the local subdomain is determined by the upwind flux (Riemann solver) and the incident field vector. This requires the information from both local and adjacent subdomains. Take the 2-D case in Fig. 1(b) as an example. The local (physical) and the adjacent (M-PML) subdomains are discretized by the 2nd order triangles and rectangles respectively for illustration purpose, although this method is implemented in 3-D for high order basis functions. Before the wave front reaches the control point (the round point) of the edge basis function (the upward solid arrow) in element 1, the incident wave does not need to be added, even though it is projected onto the basis functions in the M-PML subdomains. For example, the upward dashed arrow in Fig. 1(b) represents a basis function in element 2 in the M-PML region, and the plane wave arrives at the its control point (square point) earlier than the round point in element 1. But the flux cannot be added to the basis function (upward solid arrow) in element 1 until the wave front reaches the round point, even though the basis functions in elements 1 and 2 are coupled by the $\mathbf{L}$ matrix. Similarly, when taking the M-PML as the local subdomain, the incident wave should be subtracted from the physical subdomain to obtain the scattered field. Then, the Riemann solver links the scattered fields from M-PML and physical subdomains.

Note that in (31), $\sum_j \mathbf{L}_{ij}\mathbf{v}_{j,inc}$ is calculated only once when assembling the system matrices. At each time step, we only need to generate a new $\mathbf{F}_i$, and this computational load is negligible. In this way, the spatial connection of the basis functions from different subdomains can be pre-stored, and it is independent of the time function of the incident plane wave. An advantage of this approach is the multiple functionalities of the shared interface: It plays the roles of the SF/TF interface, the Riemann solver interface, and the non-conforming mesh connector.

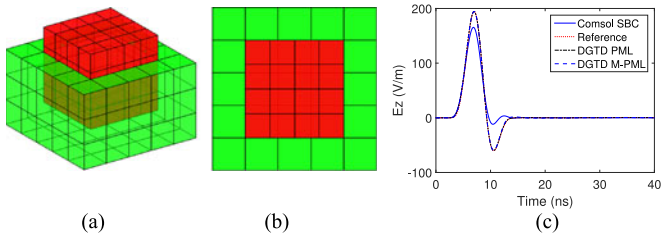

(a) (b) (c)

Fig. 2. Mesh and results. (a) Bird's-eye view and (b) top view of the mesh. (c) Results from DGTD method with PML and M-PML, COMSOL Multiphysics with SBC, and the reference from a large PEC cavity.

3. Numerical Results and Discussions

3.1 Case 1: M-PML for Full-Anisotropic Media

The field distribution in an infinite homogeneous full anisotropic medium due to an electric dipole source is studied to test the proposed M-PML. The physical region is a 2.5 m $\times$ 2.5 m $\times$ 2.5 m cube truncated by M-PML with $r(\xi, \zeta) = 0.05$ ($\xi, \zeta = x, y, z, \xi \neq \zeta$). The relative permittivity and permeability of the medium are as follows:

$$\epsilon_r = \begin{bmatrix} 1.3750 & -0.0777 & -0.4779 \\ -0.0777 & 1.0161 & 0.0990 \\ -0.4779 & 0.0990 & 1.6089 \end{bmatrix}, \quad \mu_r = \begin{bmatrix} 1.9375 & 0.2296 & 0.0765 \\ 0.2296 & 1.1562 & -0.2812 \\ 0.0765 & -0.2812 & 1.9062 \end{bmatrix}. \tag{32}$$

An electric dipole source is located at $(-0.13, -0.08, -0.1)$ m, with the polarization along the (1, 1, 1) direction. The observation point is located at (0.22, 0.14, 0.07) m. The excitation function is a Blackman-Harris Window (BHW) pulse with the characteristic frequency (f_{ch}) of 89.5 MHz. The M-PML is composed of 5th order cubic elements with the edge length of 0.8333 m (the top half of the PML region is set transparent to reveal the mesh of the physical region in Fig. 2(a)), while the physical region is discretized by the 4th order basis functions in cubic elements with the edge length of 0.625 m. Thus the mesh is non-conformal as illustrated in Fig. 2(b).

This case is also simulated in COMSOL Multiphysics, which is one of very few commercial software packages that can handle full anisotropic media in 3-D. The *Radio Frequency* module and *Electromagnetic Waves, Transient (temw)* solver are employed. The size of the cube is 2.5 m $\times$ 2.5 m $\times$ 2.5 m, and the time step length is 1 ps. The mesh sequence type is *Physics-controlled mesh* with element size option of *normal*. The scattering boundary condition (SBC) is assigned on the six outer surfaces as PML is not provided in the transient solver of COMSOL Multiphysics. The magnitude of the electric current dipole is $1.47013(-a_1 \sin(\omega t) - 2a_2 \sin(2\omega t) - 3a_3 \sin(3\omega t))\text{rect}(0, T)$, which corresponds to the normalized first order derivative of Blackman-Harris Window (BHW) pulse [24], where $a_1 = -0.488$, $a_2 = 0.145$, $a_3 = -0.010222$, $\omega = 2\pi f_{ch}$, $T = \frac{1}{f_{ch}}$, and rect$(\cdot)$ is the rectangular function.

In addition, we choose the result of a large cavity with the same anisotropic medium as a reference before the reflected waves arrive at the observation point. Fig. 2(c) demonstrates the comparison between different solvers. The agreement between the DGTD results with classical PML, M-PML and the reference is very good. That means both PML and M-PML have absorbed the out-going waves effectively with very small reflections. The relative errors (compared to the reference) are shown in Fig. 3(a). As the M-PML is "imperfect," a slightly larger reflection can be observed between 10 ns and 20 ns. However, the largest relative error is only 0.38% (-48.4 dB reflection); therefore, is accurate enough in most engineering applications.

The late-time stability, which is another key aspect to evaluate a material-based PML, is investigated for the M-PML and classical PML. The instability of the classical PML can be found from Fig. 3(b); however, the M-PML is stable. Besides simply recording the field intensity, the total energy

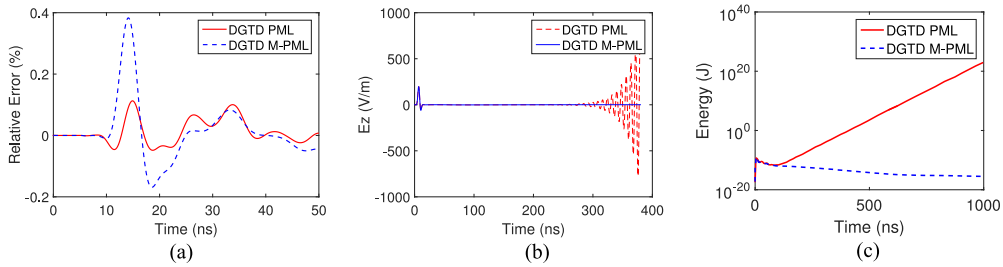

Fig. 3. Comparison between PML and M-PML. (a) Relative errors. (b) Late-time stability. (c) Total energy in the physical region.

inside the physical region is a more obvious way to evaluate the stability. As illustrated in Fig. 3(c), the energy of the physical region with the classical PML has increased after 110 ns which is a sign of instability, while for the M-PML case, the energy decays monotonically. We have tested 0.4 million time steps and the M-PML is always stable. Thus M-PML is an effective and stable absorbing boundary condition for general anisotropic media.

3.2 Case 2: Open Space Case With TS/SF Technique

In the following, we use the same case in subsection 3.1 above, but change the source to a plane wave with a BHW signal to show the effectiveness of the proposed TF/SF technique. It is incident in the XZ plane, where the direction of the wave vector is $(1/2, 0, \sqrt{3}/2)$. At $t = 0$, the wave front is at the point $(-2.08333, 0, -2.08333)$ m. With the above TF/SF technique, Fig. 4(a) shows the good agreement between the DGTD results and the analytical solution [25] for $\mathbf{E}_x$ and $\mathbf{B}_y$ at the receiver. Thus the DGTD with the TF/SF technique, combined with M-PML, can provide an effective tool for simulating electromagnetic problems in an unbounded anisotropic medium with plane wave illumination. It should be noted that the analytical solution in [25] is for frequency domain, so we have transformed it to the time domain.

3.3 Negative Refraction in YVO_4 Bicrystal

Negative refraction has attracted much attentions as this phenomenon provides the possibility to develop a superlens which can focus evanescent modes without losing image details [26]. The widely used method to achieve negative refraction is usually based on the left-hand material (LHM)[27]. However, LHM is neither a sufficient nor a necessary condition for achieving negative refraction [28]. Here we numerically simulate an alternative approach, i.e., the negative refraction and zero reflection of lightwave traveling in the YVO_4 bicrystal via the proposed anisotropic DGTD method with an M-PML of $r(\xi, \zeta) = 0.05$ $(\xi, \zeta = x, y, z, \xi \neq \zeta)$.

The YVO_4 bicystal consists of two twinning halves (denoted as sides A and B) as shown in Fig. 4(b) and investigated by [1]. The arrows indicate the orientation of the uniaxis. Both halves are nonmagnetic and have the same permittivity $\epsilon_{r,xx} = \epsilon_{r,yy} = 4.0671$, $\epsilon_{r,zz} = 5.0661$ in the principal coordinate system. Using coordinate transformation, the relative permittivities of parts A and B in the global Cartesian coordinate system are

$$\epsilon_{r,1} = \begin{bmatrix} 4.5666 & 0 & -0.4995 \\ 0 & 4.0671 & 0 \\ -0.4995 & 0 & 4.5666 \end{bmatrix}, \quad \epsilon_{r,2} = \begin{bmatrix} 4.5666 & 0 & 0.4995 \\ 0 & 4.0671 & 0 \\ 0.4995 & 0 & 4.5666 \end{bmatrix}. \tag{33}$$

We assume the incident plane is the XZ plane. For this bicrystal, an ordinary wave, whose electric field is in the y direction, will travel just as in one single material [1], and is not affected by the interface. So we only consider the extraordinary wave which can produce refraction.

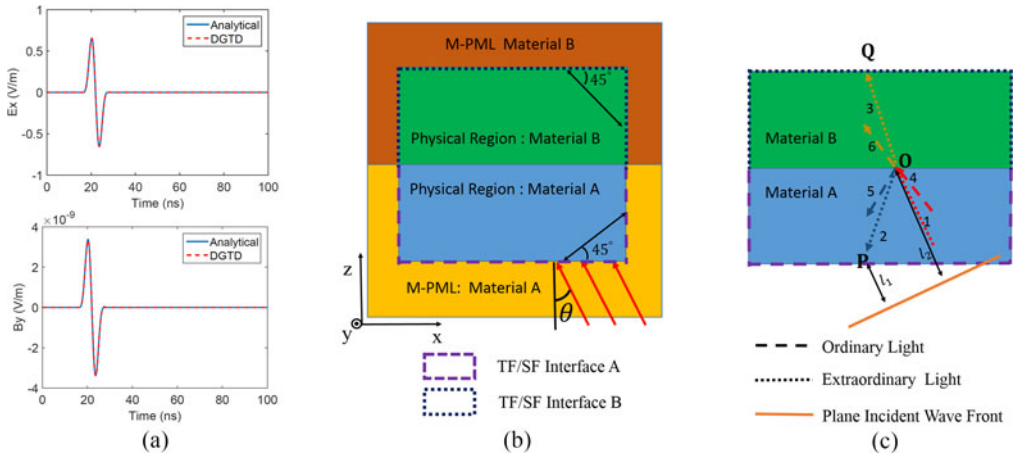

Fig. 4. Plane wave illumination validation and YVO_4 bicrystal modeling. (a) Comparison between the DGTD results and analytical solution for a plane wave traveling in an anisotropic medium. (b) Modeling YVO_4 bicrystal using the half-space TF/SF configuration and M-PML. (c) Reflection and refraction on the interface of the bicrystal.

In the DGTD simulation, the above proposed TF/SF technique is extended to half-space configuration as shown in Fig. 4(b), where the equivalent source added to the TF/SF interface A is the sum of the incident and reflected plane waves, while the equivalent source added to the TF/SF interface B is the transmitted plane wave. The M-PML is also divided into two halves, each half having the same material as the physical domain for which it is matched. In this way, the equivalent source added to the whole SF/TF interface is the same as the plane wave in infinite half space, and no approximation error will be introduced.

We define θ as the angle between the normal direction of the surface and the $\mathbf{k}$ vector ($\mathbf{k} = k_x\hat{\mathbf{x}} + k_z\hat{\mathbf{z}}$ and $\theta = \arctan k_x/k_z$). Unlike the isotropic medium, in general the $\mathbf{k}$ vector and Poynting vector have different directions in an anisotropic medium, that is, the direction of the phase velocity is different from that of energy propagation. Assume points P and Q are on the TF/SF interfaces of sides A and B, respectively. Generally, four waves exist when a plane wave impinges on the interface between two different anisotropic media [25]. They are ordinary and extraordinary waves traveling in $+z$ (transmitted waves) and $-z$ (reflected waves) directions, respectively (waves 2, 3, 5, and 6 in Fig. 4(c)). Therefore, the sum of waves 1, 2, 4, and 5 should be added to point P, and the sum of waves 3 and 6 should be added to point Q as the boundary condition. As we only consider the extraordinary wave in this case, the "incident" electric field for points P and Q can be written in a compact form, $\mathbf{E}_P = f(t-t_1)\mathbf{E}_1 + f(t-t_2)\mathbf{E}_2$ and $\mathbf{E}_Q = f(t-t_3)\mathbf{E}_3$, where f is the pulse function of the plane wave. If the materials and θ are given, $\mathbf{k}_A$, the phase velocity $\mathbf{v}_{p,A}$ and $\mathbf{E}_1$ in material A can be calculated. $\mathbf{k}_B$, $\mathbf{E}_2$ and $\mathbf{E}_3$ can be obtained from the state-variable approach for a layered medium [25], [29] because k_s (in this case $k_s = k_x$) is the horizontal component of $\mathbf{k}$, and thus remains unchanged across the interface due to the phase matching condition. Then the phase velocity in material B is known because $\mathbf{v}_{p,B} = \omega\hat{\mathbf{k}}_B/|\mathbf{k}_B|$, where $\mathbf{k}_B = |\mathbf{k}_B|\hat{\mathbf{k}}_B$. It is obvious from Fig. 4(c) that $t_1 = l_1/|\mathbf{v}_{p,A}|$, $t_2 = (l_2 + \overline{OP})/|\mathbf{v}_{p,A}|$ and $t_3 = (l_2 + \overline{OQ})/|\mathbf{v}_{p,B}|$, where l_1 and l_2 are the distances from points P and O to the wavefront at $t = 0$. Similarly, we can obtain $\mathbf{H}_P$ ($\mathbf{B}_P$) and $\mathbf{H}_Q$ ($\mathbf{B}_Q$). Note that the calculation of $\mathbf{v}_{p,B}$ and $\mathbf{v}_{p,A}$ is in the frequency domain. Because the material is non-dispersive, all the frequency components of the wideband plane wave have the same speed.

In the DGTD numerical simulation, the source is a plane wave with a BHW signal with the characteristic frequency of $f_{ch} = 363.8$ THz. The sizes of both twining sides A and B are $4l \times 4l \times 4l$, and the thickness of the PML is l in all the directions, where $l = \frac{1}{f_{ch}}$. All the cubes in the mesh are 4th order elements with the edge length of l.

Two cases are simulated to show normal and negative refractions. The incidence angles of the $\mathbf{k}$ vectors are $\theta = -10^\circ$ and $\theta = 0^\circ$, respectively. As the z component of the Poynting vector (S_z) is

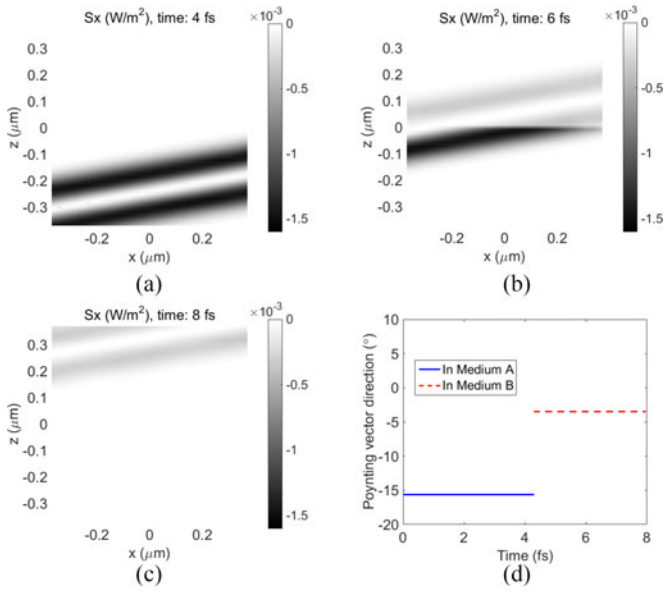

Fig. 5. Normal refraction ($\theta = -10^\circ$). x component of Poynting vector at (a) $t = 4$ fs. (b) $t = 6$ fs. (c) $t = 8$ fs. (d) Poynting vector direction on a wave front point versus time.

continuous across the interface ($z = 0$), the x component of the Poynting vector (S_x) determines whether it is normal (positive) or negative refraction. If S_x has a sign change across the interface, the incident and refraction energy flows lie on the same side of the normal of the interface. This phenomenon is the negative refraction; otherwise, it is normal refraction. In Fig. 5(a)–(c) for $\theta = -10^\circ$, it can be observed that S_x is always negative, thus it is normal refraction. However, in Fig. 6(a), (b) and (c) for $\theta = 0^\circ$, S_x changes from negative to positive across the interface, which is negative refraction. This conclusion can be also drawn from Fig. 5(d) and (d). They record the Poynting vector direction of a point on the wave front versus time. The point is located at (0, 0, -6*l*) at the time $t = 0$. In Fig. 6(d), the Poynting vector of this wave front point changes from a negative angle in medium A to a positive angle in medium B, so it is negative refraction, while Fig. 5(d) shows normal refraction. In addition, no reflected waves are found, which agrees with the description of zero reflection of this bycrystal in [28].

More different values of θ have been tested, and the comparison between the numerical results and the analytical solution is shown in Fig. 7(a). The incident and refractive angles of the energy agree very well, and the errors are all less than 1%. A point lies in the first or the third quadrant represents normal refraction, while a point in the second or fourth quadrant represents negative refraction. For this YVO_4 bicrystal, the negative refraction occurs when the incident angel (respect to energy) is within the region $[-12.34^\circ, 0^\circ]$.

The refraction property can be also interpreted physically with the equi-frequency contour (EFC) in the k space [30]. The dispersion relationship of the YVO_4 bicrystal is

$$\left(\frac{\omega}{c}\right)^2 = \frac{(k_x \cos\alpha + k_z \sin\alpha)^2}{\epsilon_{zz}} + \frac{(k_x \sin\alpha - k_z \cos\alpha)^2}{\epsilon_{xx}}. \tag{34}$$

It is obvious that the wave vector k forms an ellipse as shown in Fig. 7(b). For example, if the incident angle of the wave vector in medium A is $k_{A,1}$, we can draw a tangent line of the ellipse at the end point of $k_{A,1}$, while the Poynting vector is perpendicular to this line denoted as $s_{A,1}$. As the tangential component of the wave vector is continuous across the interface, we can easily obtain the wave vector $k_{B,1}$ and Poynting vector $s_{B,1}$ in medium B. As $s_{B,1}$ and $s_{A,1}$ both have positive x components, normal (positive) refraction is achieved. By the same token, abnormal (negative) refraction appears between $s_{B,2}$ and $s_{A,2}$.

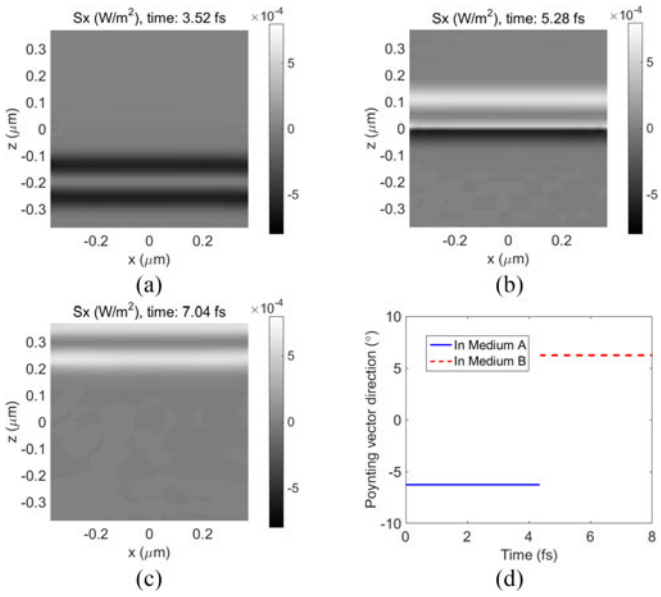

Fig. 6. Negative refraction ($\theta = 0^\circ$). x component of Poynting vector at (a) $t = 3.52$ fs. (b) $t = 5.28$ fs. (c) $t = 7.04$ fs. (d) Poynting vector direction on a wave front point versus time.

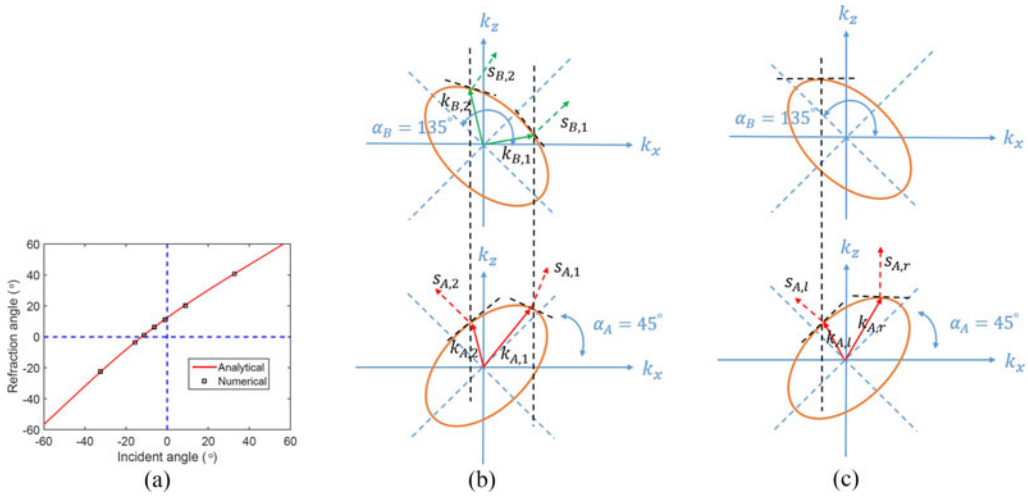

Fig. 7. Analysis of the incident and refraction angles for YVO_4 bicrystal. (a) Numerical (DGTD) and analytical incident and refractive angles. (b) Negative and positive refractions examples and (c) negative refraction range from EFC approach.

From the EFC of the YVO_4 bicrystal, it can be observed that the refraction property is a function of the incident angle of Poynting vector s_A. Only if s_A is between $s_{A,l}$ and $s_{A,r}$ (k_A is between $k_{A,l}$ and $k_{A,r}$) as shown in Fig. 7(c), it is negative refraction. In addition, the larger range of incident angles of negative refractions can be expected if larger difference between the long and short axes of the ellipse is achieved (i.e., the large different between ϵ_{xx} and ϵ_{zz}).

4. Conclusion

In this research, the isotropic DGTD method has been extended to allow full anisotropic media. To achieve this goal, an unsplit-field, stable time domain Maxwellian multiaxial PML is proposed to truncate the anisotropic media. An anisotropic Riemann solver is employed to obtain the numerical flux between adjacent subdomains. An improved TF/SF technique is developed for the vector basis functions and non-conformal mesh in the DGTD method when the source is a plane wave. The effectiveness of these new approaches is validated by several numerical cases. The negative refraction of lightwave in a 3-D YVO_4 bicrystal is modeled and simulated with high accuracy for the first time via the anisotropic DGTD method after extending the proposed TF/SF technique to half-space configuration.

This work can be extended to simulate more complex geometries, for example, beam displacer and etc. And it also provides a basis for the further study of complex anisotropic media, such as graphene with gyrotropy.

Acknowledgment

The authors thank Prof. Y. Zhang for suggesting to simulate the YVO_4 bicrystal in this work.

References

[1] Y. Zhang, B. Fluegel, and A. Mascarenhas, "Total negative refraction in real crystals for ballistic electrons and light," *Phys. Rev. Lett*, vol. 91, no. 15, 2003, Art. no. 157404.
[2] Y. Du, M. He, X. Chen, W. Wang, and D. Zhang, "Uniaxial crystal slabs as amphoteric-reflecting media," *Phys. Rev. B*, vol. 73, no. 24, 2006, Art. no. 245110.
[3] L. E. Tobón, Q. Ren, and Q. H. Liu, "A new efficient 3-D discontinuous Galerkin time domain (DGTD) method for large and multiscale electromagnetic simulations," *J. Comput. Phys.*, vol. 283, pp. 374–387, 2015.
[4] Q. Ren, L. E. Tobón, Q. Sun, and Q. H. Liu, "A new 3-D non-spurious discontinuous Galerkin spectral element time domain (DG-SETD) method for Maxwell's equations," *IEEE. Trans. Antennas Propag.*, vol. 63, no. 6, pp. 2585–2594, Jun. 2015.
[5] Q. Ren, Q. Sun, L. Tobón, Q. Zhan, and Q. H. Liu, "EB scheme based hybrid SE-FE DGTD method for multiscale EM simulations," *IEEE. Trans. Antennas Propag.*, vol. 64, no. 9, pp. 4088–4091, Sep. 2016.
[6] J. Chen, L. E. Tobón, M. Chai, J. A. Mix, and Q. H. Liu, "Efficient implicit–explicit time stepping scheme with domain decomposition for multiscale modeling of layered structures," *IEEE Trans. Compon. Packag. Manuf. Technol.*, vol. 1, no. 9, pp. 1438–1446, Sep. 2011.
[7] J. Alvarez, L. D. Angulo, A. R. Bretones, and S. G. Garcia, "3-D discontinuous Galerkin time domain method for anisotropic materials," *IEEE Antennas Wireless Propag. Lett.*, vol. 11, pp. 1182–1185, 2012.
[8] Z. S. Sacks, D. M. Kingsland, R. Lee, and J.-F. Lee, "A perfectly matched anisotropic absorber for use as an absorbing boundary condition," *IEEE. Trans. Antennas Propag.*, vol. 43, no. 12, pp. 1460–1463, Dec. 1995.
[9] S. D. Gedney, "An anisotropic perfectly matched layer-absorbing medium for the truncation of FDTD lattices," *IEEE. Trans. Antennas Propag.*, vol. 44, no. 12, pp. 1630–1639, Dec. 1996.
[10] A. P. Zhao, J. Juntunen, and A. V. Raisanen, "Generalized material-independent PML absorbers for the FDTD simulation of electromagnetic waves in arbitrary anisotropic dielectric and magnetic media," *IEEE Microwave Guided Wave Lett.*, vol. 8, no. 2, pp. 52–54, Feb. 1998.
[11] F. Teixeira and W. Chew, "A general approach to extend berenger's absorbing boundary condition to anisotropic and dispersive media," *IEEE. Trans. Antennas Propag.*, vol. 46, no. 9, pp. 1386–1387, Sep. 1998.
[12] Q. H. Liu, "PML and PSTD algorithm for arbitrary lossy anisotropic media," *IEEE Microwave Guided Wave Lett.*, vol. 9, no. 2, pp. 48–50, Feb. 1999.
[13] G.-X. Fan and Q. H. Liu, "A strongly well-posed PML in lossy media," *IEEE Antennas Wireless Propag. Lett.*, vol. 2, no. 1, pp. 97–100, 2003.
[14] Q. Ren, L. E. Tobón, and Q. H. Liu, "A new 2-D non-spurious discontinuous Galerkin finite element time domain (DG-FETD) method for Maxwell's equations," *Prog. Electromag. Res.*, vol. 143, pp. 385–404, 2013.
[15] A. Peterson, S. Ray, and R. Mittra, *Computational Methods for Electromagnetics*, vol. 24. New York, NY, USA: IEEE, 1998.
[16] J. Hesthaven and T. Warburton, "Discontinuous Galerkin methods for the time-domain Maxwell's equations," *ACES Newslett*, vol. 19, no. EPFL-ARTICLE-190449, pp. 10–29, 2004.
[17] D. A. Kopriva and G. Gassner, "On the quadrature and weak form choices in collocation type discontinuous Galerkin spectral element methods," *SIAM J. Sci. Comput.*, vol. 44, no. 2, pp. 136–155, 2010.
[18] J. Hesthaven and T. Warburton, "Nodal high-order methods on unstructured grids—I: Time-domain solution of Maxwell's equations," *J. Comput. Phys.*, vol. 181, no. 1, pp. 186–221, 2002.
[19] P. Silvester and R. Ferrari, *Finite Elements for Electrical Engineers*. Cambridge, U.K.: Cambridge Univ. Press, 1996.

[20] K. C. Meza-Fajardo and A. S. Papageorgiou, "A nonconvolutional, split-field, perfectly matched layer for wave propagation in isotropic and anisotropic elastic media: stability analysis," *Bull. Seismol. Soc. Amer.*, vol. 98, no. 4, pp. 1811–1836, 2008.
[21] C. Zeng, J. Xia, R. D. Miller, and G. P. Tsoflias, "Application of the multiaxial perfectly matched layer (M-PML) to near-surface seismic modeling with Rayleigh waves," *Geophys.*, vol. 76, no. 3, pp. T43–T52, 2011.
[22] K. C. Meza-Fajardo and A. S. Papageorgiou, "On the stability of a non-convolutional perfectly matched layer for isotropic elastic media," *Soil Dyn. Earthq. Eng.*, vol. 30, no. 3, pp. 68–81, 2010.
[23] K. C. Meza-Fajardo and A. S. Papageorgiou, "Study of the accuracy of the multiaxial perfectly matched layer for the elastic-wave equation," *Bull. Seismol. Soc. Amer.*, vol. 102, no. 6, pp. 2458–2467, 2012.
[24] Q. H. Liu, "An FDTD algorithm with perfectly matched layers for conductive media," *IEEE Microwave Guided Wave Lett.*, vol. 14, no. 2, pp. 134–137, 1997.
[25] W. C. Chew, *Waves and Fields in Inhomogeneous Media*, vol. 522. New York, NY, USA: IEEE, 1995.
[26] J. B. Pendry, "Negative refraction makes a perfect lens," *Phys. Rev. Lett.*, vol. 85, no. 18, pp. 3966–3969, 2000.
[27] R. A. Shelby, D. R. Smith, and S. Schultz, "Experimental verification of a negative index of refraction," *Science*, vol. 292, no. 5514, pp. 77–79, 2001.
[28] C. M. Krowne and Y. Zhang, *Physics of Negative Refraction and Negative Index Materials*. Berlin, Germany: Springer, 2007.
[29] M. A. Morgan, D. Fisher, and E. Milne, "Electromagnetic scattering by stratified inhomogeneous anisotropic media," *IEEE. Trans. Antennas Propag.*, vol. AP-35, no. 2, pp. 191–197, Feb. 1987.
[30] Z. Liu, Z. Lin, and S. Chui, "Negative refraction and omnidirectional total transmission at a planar interface associated with a uniaxial medium," *Phys. Rev. B,*, vol. 69, no. 11, 2004, Art. no. 115402.